

# Issues in Modeling Heterogeneous Deformations in Polycrystalline Metals using Multiscale Approaches

Paul R. Dawson<sup>1</sup>, Donald E. Boyce<sup>2</sup> and Ronald Rogge<sup>3</sup>

**Abstract:** Computational mechanics provides a powerful environment for modeling the evolution of material structure during deformation processes and for associating that evolution with changes to the mechanical properties. In this paper, we illustrate a two-scale formulation that links the mechanical loading applied at the scale of a component (the continuum scale) to the responses of the material at the scale of the crystals that comprise it (the crystal scale). Employing the capabilities offered by computational mechanics, we can better understand how heterogeneity of deformation arising at both the continuum and crystal scales influences the behaviors observed experimentally. Such an understanding is central to improving the performance of engineering alloys.

**keyword:** Finite element, plasticity, polycrystals, multiscale, in situ diffraction

## 1 Focus and Scope

Twenty-five years ago, the modeling of material property evolution was in its infancy. Research on the topic was motivated in part by materials processing, a subject central to our manufacturing competitiveness. NSF, especially through the efforts of Dr. Clifford Astill in the Solid Mechanics Program, supported research to develop simulation methodologies with a rigorous mechanics foundation. Early efforts focused on the modeling of processes such as hardening and damage formation using state variables with only indirect links to the material structure. Over time, the modeling capabilities matured into powerful tools. Simplistic representations of state were replaced by ones with direct association to observables of the material, with crystallographic texture being a notable example. Experimental methods progressed

from coarse measurements of resultant forces and gross shape changes to sophisticated diffraction measurements under *in situ* loading. Numerical formulations advanced from crude 2D approximations to detailed 3D renderings of the material and the processes that alter it. Recently, efforts have been devoted to the development of methodologies that can bridge physical length scales. At one end of the spectrum of scales is the process; at the other the building blocks of the material (potentially to the atoms themselves). In the spirit of this field, we present a formulation that bridges the crystal scale, where elastic and plastic processes can be described on a more basic level, and continuum scale, where the boundary value problem associated with the mechanical loading of a mechanical component is defined. The methods trace their roots to the early support of Dr. Astill over a quarter century ago (Dawson (1984, 1987); Eggert and Dawson (1987); Mathur and Dawson (1987, 1989); Beaudoin, Dawson, Mathur, Kocks, and Korzekwa (1994)).

Polycrystal elastoplasticity is a microstructural approach for modeling the mechanical behavior of crystalline solids. Models of this type have two basic parts: the single crystal equations and the relations for averaging crystal quantities over polycrystalline aggregates. The latter in essence define the grain interactions allowed by the model. As the polycrystal properties are derived from the collective responses of crystals comprising a polycrystal, they are strongly influenced by both the single crystal behavior and the nature of the grain interactions. Single crystal mechanical properties depend on the orientation of the crystal's atomic lattice. Thus, the strength of the mechanical anisotropy of a polycrystal depends on that of the individual crystals, on the lattice orientation distribution, and on the methodology for averaging single crystal responses over the distribution. At the crystal scale, deformation under load typically is spatially heterogeneous; averaging over those grains that comprise a polycrystal tends to dampen this variability, but the aggregate response of the polycrystal can remain highly

---

<sup>1</sup> Sibley School of Mechanical and Aerospace Engineering, Cornell University, Ithaca, NY, USA 14853

<sup>2</sup> Sibley School of Mechanical and Aerospace Engineering, Cornell University, Ithaca, NY, USA 14853

<sup>3</sup> Neutron Program for Materials Research, National Research Council of Canada, Chalk River, Ontario, Canada

anisotropic. In this paper, we take the polycrystal response to be the same as that of the continuum, giving two effective length scales: the crystal (microscopic) and the continuum (macroscopic).

As mentioned above, the early efforts to accommodate the influence of complex microscopic process in macroscopic models was by means of variables that are indirectly associated with the microscopic state. For example, the variable for isotropic strength used in many constitutive models is proportional to the (square root of the) dislocation density. Its evolution with straining is determined by correlations with measured values of the strength, rather than by direct measurement of dislocation densities. Multiscale formulations offer the potential to explicitly account for processes at microscopic scales in the assessment of properties at macroscopic scale. The intent of multiscale modeling often is to inform the macroscopic model of the properties expected as a consequence of behaviors at microscopic scale, as well as to inform the microscopic scale of the loading conditions imposed at the macroscopic scale. This necessitates the movement of information regarding the stress and deformation between micro and macro scales as part of any computations that employ the formulation.

A number of issues arise in implementing a finite element-based multiscale approach related the consistency of responses across the scales. These include methods for projecting macroscale motion onto microscale ensembles, for defining consistent measures of stiffness at both scales, and for determining valid samples of the microstructure. We address these in the context of simulating neutron diffraction experiments performed on a mechanical component under *in situ* loading. We begin with a summary of the model equations. We then present simulation results associated with two types of experiments, ones having macroscopically homogeneous deformations (tension tests) and ones having macroscopically inhomogeneous deformations (bending tests). Finally, we discuss these in terms of the issues mentioned above. The underlying intent is to illustrate by example progress made in the area of computational mechanics that benefitted from Dr. Astill's strong support early in its development.

## 2 Elastic and Plastic Behaviors of Single Crystals

We refer the reader to two references, the books edited by Kocks, Tome, and Wenk (1998) and by Raabe, Roters,

Barlat, and Chen (2004) for comprehensive coverage of the topic. The developments used here for both the continuum and crystals scales follows the procedure summarized in chapters within those references. The physical domain (volume) of a polycrystalline body is designated as  $\mathcal{B}$  and its boundary as  $\partial\mathcal{B}$ . Coordinates of points within this domain are given by  $\mathbf{x}$ . The velocity field over the domain is given by  $\mathbf{u}(\mathbf{x})$  and its spatial gradient, the velocity gradient, as  $\mathbf{l}(\mathbf{x})$ . The polycrystalline domain is divided into crystal subdomains that fill the domain without overlapping. The Cauchy stress within a crystal (called the crystal or micro stress) is designated as  $\boldsymbol{\sigma}(\mathbf{x})$  and the traction on a surface within or on the boundary of  $\mathcal{B}$  as  $\mathbf{t}$ . The following notation convention is adopted: lower case variables associated with either the stress or the motion apply to quantities at the crystal scale while upper case letters apply to quantities at the continuum scale; plain fonts are used for scalars, math bold fonts are used for vectors, and math sans serif fonts are used for higher-order tensors or matrices; superscript symbols,  $\flat$ ,  $\sharp$  and  $\star$ , refer to mapping over a change of configuration; superscript  $\alpha$  refers to a particular slip system; and, superscript  $\prime$  refers to the deviatoric part of a tensor. A superposed dot indicates material time differentiation.

The material we are modeling is an austenitic stainless steel that is essentially single phase (face-centered cubic). We assume that in the regime of loading (room temperature and quasi-static) the inelastic deformation is dominated by crystallographic slip. At the level of an individual crystal, the motion consists of elastic and plastic parts, as well as a rotation. The plastic deformation occurs through crystallographic slip between atomic planes of the crystal lattice. The elastic deformations are associated with lengthening or shortening of the interatomic distances. This description gives rise to the representation of the kinematics of crystal deformations with a multiplicative decomposition of the deformation gradient  $\mathbf{f}$

$$\mathbf{f} = \mathbf{f}^{\flat} \mathbf{f}^{\star} \mathbf{f}^{\sharp} = \mathbf{v}^{\flat} \mathbf{r}^{\star} \mathbf{f}^{\sharp} \quad (1)$$

where  $\mathbf{f}^{\sharp}$  is the purely plastic part of  $\mathbf{f}$  arising from slip,  $\mathbf{f}^{\star}$  is the lattice rotation which may be written as  $\mathbf{r}^{\star}$ , and  $\mathbf{f}^{\flat}$  is the elastic part of  $\mathbf{f}$ . The deformation gradient  $\mathbf{f}^{\sharp}$  can be used to define an intermediate configuration,  $\hat{\mathcal{B}}$ , which is a relaxed configuration obtained by unloading without rotation from the current configuration  $\mathcal{B}$ . Using this interpretation of  $\hat{\mathcal{B}}$ , the symmetric left elastic stretch tensor,  $\mathbf{v}^{\flat}$ , is introduced. For the case of small elastic strains,

$\mathbf{v}^b = \mathbf{I} + \mathbf{e}^b$ , where  $\|\mathbf{e}^b\| \ll 1$  and  $\mathbf{I}$  is the second order identity tensor. From this decomposition, the kinematics then are expressed in rate form as

$$\dot{\mathbf{l}} = \dot{\mathbf{f}}\mathbf{f}^{-1} = \mathbf{d} + \mathbf{w} \quad (2)$$

where  $\mathbf{d}$  is the deformation rate tensor and  $\mathbf{w}$  the spin tensor, expressed in the current configuration  $\mathcal{B}$ . These terms may be split into spherical

$$\text{tr}(\mathbf{d}) = \text{tr}(\dot{\mathbf{e}}^b) \quad (3)$$

and deviatoric parts

$$\mathbf{d}' = \dot{\mathbf{e}}^{b'} + \hat{\mathbf{d}}^{\#'} + \mathbf{e}^{b'} \hat{\mathbf{w}}^{\#} - \hat{\mathbf{w}}^{\#} \mathbf{e}^{b'} \quad (4)$$

and

$$\mathbf{w} = \hat{\mathbf{w}}^{\#} + \mathbf{e}^{b'} \hat{\mathbf{d}}^{\#'} - \hat{\mathbf{d}}^{\#'} \mathbf{e}^{b'} \quad (5)$$

where  $\mathbf{d}'$  and  $\mathbf{e}^{b'}$  are the deviatoric components of  $\mathbf{d}$  and  $\mathbf{e}^b$ , respectively. The  $\hat{\cdot}$  superscript indicates mapping forward by  $\mathbf{r}^*$  according to

$$\hat{\mathbf{w}}^{\#} = \mathbf{r}^* \mathbf{w}^{\#} \mathbf{r}^{*\text{T}} \quad \text{and} \quad \hat{\mathbf{d}}^{\#'} = \mathbf{r}^* \mathbf{d}^{\#'} \mathbf{r}^{*\text{T}} \quad (6)$$

to define the plastic deformation rate tensor,  $\hat{\mathbf{d}}^{\#'}$ , and the plastic spin tensor,  $\hat{\mathbf{w}}^{\#}$ , in the relaxed configuration  $\hat{\mathcal{B}}$ .

The elastic response follows a linear relation

$$\boldsymbol{\tau} = \mathbf{c} \mathbf{e}^b \quad \text{where} \quad \mathbf{c} = \mathbf{c}(\mathbf{r}) \quad (7)$$

where  $\mathbf{c}$  is the tensor containing elastic moduli for cubic crystal symmetry which depends on the orientation of the crystallographic lattice,  $\mathbf{r}$ . The Kirchhoff stress,  $\boldsymbol{\tau}$ , is related to the Cauchy stress,  $\boldsymbol{\sigma}$ , through  $\boldsymbol{\tau} = \beta \boldsymbol{\sigma}$ , where  $\beta = \det(\mathbf{v}^b)$ .

The viscoplastic flow rule is derived from the crystallographic slip and is defined as

$$\hat{\mathbf{l}}^{\#} = \hat{\mathbf{d}}^{\#'} + \hat{\mathbf{w}}^{\#} = \dot{\mathbf{r}}^* \mathbf{r}^{*\text{T}} + \sum_{\alpha} \dot{\gamma}^{\alpha} (\hat{\mathbf{b}}^{\alpha} \otimes \hat{\mathbf{m}}^{\alpha}) \quad (8)$$

where  $\hat{\mathbf{b}}^{\alpha}$  is the slip direction and  $\hat{\mathbf{m}}^{\alpha}$  the normal to the slip plane along the  $\alpha$ -slip system in configuration  $\hat{\mathcal{B}}$ . The assumed slip systems for the FCC crystals are the 12 systems with  $\langle 110 \rangle$  directions and  $\langle 111 \rangle$  normals. The symmetric and skew symmetric parts of the plastic velocity gradient,  $\hat{\mathbf{d}}^{\#'}$  and  $\hat{\mathbf{w}}^{\#}$ , respectively, are defined as

$$\hat{\mathbf{d}}^{\#'} = \sum_{\alpha} \dot{\gamma}^{\alpha} \hat{\mathbf{p}}^{\alpha}(\mathbf{r}) \quad \text{and} \quad \hat{\mathbf{w}}^{\#} = \dot{\mathbf{r}}^* \mathbf{r}^{*\text{T}} + \sum_{\alpha} \dot{\gamma}^{\alpha} \hat{\mathbf{q}}^{\alpha}(\mathbf{r}) \quad (9)$$

where

$$\hat{\mathbf{p}}^{\alpha}(\mathbf{r}) = \text{sym}(\hat{\mathbf{b}}^{\alpha} \otimes \hat{\mathbf{m}}^{\alpha}) \quad \text{and} \quad \hat{\mathbf{q}}^{\alpha}(\mathbf{r}) = \text{skw}(\hat{\mathbf{b}}^{\alpha} \otimes \hat{\mathbf{m}}^{\alpha}) \quad (10)$$

The plastic shearing rate on the  $\alpha$ -slip system,  $\dot{\gamma}^{\alpha}$ , is related to the crystal stress by the power law relation

$$\dot{\gamma}^{\alpha} = \dot{\gamma}_0 \left( \frac{|\tau^{\alpha}|}{g} \right)^{\frac{1}{m}} \text{sgn}(\tau^{\alpha}) = f(\tau^{\alpha}, g) \quad (11)$$

where  $g$  is the slip system hardness,  $\dot{\gamma}_0$  is a reference shear rate, and  $m$  is the rate sensitivity of slip. The resolved shear stress,  $\tau^{\alpha}$ , is the plastic work rate conjugate to  $\dot{\gamma}^{\alpha}$ , and is the projection of the deviatoric part of the Kirchhoff stress,  $\boldsymbol{\tau}'$  on the  $\alpha$ -slip system as

$$\tau^{\alpha} = \text{tr}(\hat{\mathbf{p}}^{\alpha} \boldsymbol{\tau}') \quad (12)$$

The slip system hardness,  $g$ , is assumed to be the same for all slip systems and evolves according to the following hardening rule

$$\dot{g} = h_0 \left( \frac{g_s(\dot{\gamma}) - g}{g_s(\dot{\gamma}) - g_0} \right)^n \dot{\gamma} \quad (13)$$

where

$$g_s(\dot{\gamma}) = g_1 \left( \frac{\dot{\gamma}}{\dot{\gamma}_1} \right)^{m'} \quad \text{and} \quad \dot{\gamma} = \sum_{\alpha} |\dot{\gamma}^{\alpha}|. \quad (14)$$

Here,  $\dot{\gamma}^{\alpha}$  is the net shear strain rate in the crystal,  $g_s(\dot{\gamma})$  is the saturation hardness, and  $h_0$ ,  $g_0$ ,  $n$ ,  $g_1$ ,  $\dot{\gamma}_1$ , and  $m'$  are slip system hardening parameters, which are the same for all slip systems. The lattice orientation evolves as a consequence of the spin, and is given by

$$\dot{\mathbf{r}} = \mathbf{v} = \frac{1}{2} \boldsymbol{\omega} + (\boldsymbol{\omega} \cdot \mathbf{r}) \mathbf{r} + \boldsymbol{\omega} \times \mathbf{r} \quad (15)$$

where

$$\boldsymbol{\omega} = \text{vect} \left( \hat{\mathbf{w}}^{\#} - \sum_{\alpha} \dot{\gamma}^{\alpha} \hat{\mathbf{q}}^{\alpha} \right) \quad (16)$$

### 3 Averaging over Polycrystals

We next present the equations to link the scales by relating the analogous quantities defined for each. From this we draw the need to make assumptions to be able to build a multiscale model that explicitly includes both. It may be difficult to *a priori* establish whether or not

such assumptions are reasonable, although some may be known to lead to either upper or lower bounds on the macro properties.

Macroscopic quantities analogous to the microscopic velocity gradient and Cauchy stress are defined using formulae that deliver representative values for the domain  $\mathcal{B}$  by considering the velocity and traction distribution over the boundary  $\partial\mathcal{B}$ . The representative value of the velocity gradient is based on the distribution of velocity over the boundary; the representative value of the Cauchy stress is based on the distribution of traction over the boundary. One need not know the details of how each of the corresponding microscopic quantities is distributed over the domain to determine the macroscopic values. The macro velocity gradient,  $\mathbf{L}$ , defined this way is:

$$\mathbf{L} = \frac{1}{\mathcal{B}} \int_{\partial\mathcal{B}} \mathbf{n} \otimes \mathbf{u} \, d\Gamma \quad (17)$$

and the macro stress,  $\mathbf{\Sigma}$ , is:

$$\mathbf{\Sigma} = \frac{1}{\mathcal{B}} \int_{\partial\mathcal{B}} \mathbf{x} \otimes \mathbf{t} \, d\Gamma \quad (18)$$

where  $\mathbf{n}$  is the unit vector normal to the boundary,  $\partial\mathcal{B}$ .

It is also possible to construct volumetric averages of the micro scale velocity gradient and Cauchy stress as:

$$\bar{\mathbf{l}} = \langle \mathbf{l} \rangle = \frac{1}{\mathcal{B}} \int_{\mathcal{B}} \mathbf{l} \, d\mathcal{B} \quad (19)$$

and

$$\bar{\boldsymbol{\sigma}} = \langle \boldsymbol{\sigma} \rangle = \frac{1}{\mathcal{B}} \int_{\mathcal{B}} \boldsymbol{\sigma} \, d\mathcal{B} \quad (20)$$

If

$$\mathbf{\Sigma} = \bar{\boldsymbol{\sigma}} \quad \text{and} \quad \mathbf{L} = \bar{\mathbf{l}} \quad (21)$$

then the responses at the continuum and crystal scales can be directly associated with each other. However, for this to be true, the stress and velocity gradient fields must be smooth. This is evident from derivations (see Hill (1979) and Nemat-Nasser and Hori (1999)) that employ the divergence theorem to prove the equivalence of  $\mathbf{L}$  to  $\bar{\mathbf{l}}$  and of  $\mathbf{\Sigma}$  to  $\bar{\boldsymbol{\sigma}}$ . Should the crystal scale quantities lack the smoothness demanded by the divergence theorem, we are not guaranteed that the volumetric averages of the crystal scale quantities will be equivalent to the associated quantities at the continuum scale. The implication of this is that the properties that relate the stress and (rates of) deformation are specific to the scale, a distinction that may or may not be significant. We will discuss this point in the context of the bending application later.

## 4 Finite Element Formulation for Crystal and Continuum Scales

To consider the influence of the potential difference between the macro stress and the volume averaged micro stress, we examine the formulations for solving the field equations for each scale. The formulation for each builds from the weak form of the equilibrium equations.

### 4.1 Crystal-scale formulation

For the crystal scale, the weak form is:

$$R_u = - \int_{\mathcal{B}} \text{tr} \left( \boldsymbol{\sigma}'^T \text{grad} \boldsymbol{\Psi} \right) d\mathcal{B} + \int_{\mathcal{B}} \pi \text{div} \boldsymbol{\Psi} d\mathcal{B} + \int_{\partial\mathcal{B}} \mathbf{t} \cdot \boldsymbol{\Psi} d\Gamma + \int_{\mathcal{B}} \mathbf{l} \cdot \boldsymbol{\Psi} d\mathcal{B} \quad (22)$$

where the deviatoric Cauchy stress,  $\boldsymbol{\sigma}'$ , and mean stress (negative of the pressure,  $\pi$ ) sum to the total Cauchy stress:

$$\boldsymbol{\sigma} = \boldsymbol{\sigma}' - \pi \mathbf{I} \quad (23)$$

Traction or velocity is specified over the boundary. Following a standard Galerkin methodology,  $\boldsymbol{\Psi}$  are the weights that span the same space as the trial functions for the velocity.

We note for a velocity-based formulation, the velocity field is forced to be continuous everywhere via the properties of the trial functions. However, the stress field typically will not be continuous across element boundaries. Thus, one should not expect that an average stress computed over the domain at the crystal scale will necessarily render the continuum stress, as defined by Equation 20, as the necessary smoothness conditions may not be satisfied.

The stress is replaced ultimately with the velocity field through introduction of the constitutive equations and the kinematic relation defining the velocity gradient. The first step in this process is to introduce a difference expression for the elastic strain rate as

$$\left\{ \dot{\mathbf{e}}^b \right\} = \frac{1}{\Delta t} \left( \left\{ \mathbf{e}^b \right\} - \left\{ \mathbf{e}_0^b \right\} \right) \quad (24)$$

This is separated into the volumetric part

$$-\pi = \frac{\kappa \Delta t}{\beta} \text{tr} \left\{ \mathbf{d} \right\} + \frac{\kappa}{\beta} \text{tr} \left\{ \mathbf{e}_0^b \right\} \quad (25)$$

and the deviatoric part

$$\{d'\} = \frac{1}{\Delta t} \{e^{b'}\} + \{\hat{d}^\# \} + [\hat{w}^\#] \{e^{b'}\} - \frac{1}{\Delta t} \{e_0^{b'}\} \quad (26)$$

Inverting the equation for the elastic behavior in Eq 7,

$$\{e^{b'}\} = [c]^{-1} \{\tau'\} \quad (27)$$

and combining it with a relation obtained from merger of Eq 9, 11 and 12

$$\{\hat{d}^\# \} = [m] \{\tau'\} \quad (28)$$

where

$$[m] = \sum_{\alpha} \left( \frac{f(\tau^\alpha, g)}{\tau^\alpha} \right) \{p^\alpha\} \{p^\alpha\}^T \quad (29)$$

results in a matrix equation for the stress in terms of the total deformation rate

$$\{\sigma'\} = [s] \left( \{d'\} - \{h\} \right) \quad (30)$$

where:

$$[s]^{-1} = \frac{\beta}{\Delta t} [c]^{-1} + \beta [m] \quad (31)$$

and

$$\{h\} = [\hat{w}^\#] \{e^{b'}\} - \frac{1}{\Delta t} \{e_0^{b'}\} \quad (32)$$

Equations 25 and 30 are substituted into Eq 22 to eliminate the explicit appearance of the stress.

#### 4.2 Continuum scale formulation

Similarly, for the macro scale, the weak form is:

$$R_u = - \int_{\mathcal{B}} \text{tr}(\Sigma'^T \text{grad} \Psi) d\mathcal{B} + \int_{\mathcal{B}} \Pi \text{div} \Psi d\mathcal{B} + \int_{\partial \mathcal{B}} \mathbf{T} \cdot \Psi d\Gamma + \int_{\mathcal{B}} \mathbf{j} \cdot \Psi d\mathcal{B} \quad (33)$$

where the macro Cauchy stress again has been decomposed into a pressure,  $\Pi$ , and a deviatoric part,  $\Sigma'$ :

$$\Sigma = \Sigma' - \Pi \mathbf{I} \quad (34)$$

$\Psi$  are the weights.

We proceed to a matrix equation for the deviatoric stress in terms of the deformation rate, now for the macroscopic quantities, in the same fashion as for the crystal scale. An equation similar in structure to Equation 30 is assumed to exist at the macro level of the form:

$$\{\Sigma'\} = [S] \left( \{D'\} - \{H\} \right) \quad (35)$$

Relating the micro and macro constitutive equations can be accomplished in a variety of ways. If the  $[S]$  matrix is determined from computed responses of the micro scale body (and employing the boundary-based definitions of macro stress and velocity gradient), a suite of straining directions is necessary. This would be costly, but in theory, feasible. If instead, one chooses to invoke a number of constitutive assumptions, the procedure for assessing the macro scale properties from the aggregate responses of the micro scale constituents can be streamlined considerably. Two basic assumptions are needed:

1. the volumetric average of the micro stresses is approximately the macro stress, and
2. a mean field approximation regarding the distribution of stress or deformation rate over the micro scale domain may be made.

For example, if we assume the specific condition that  $\mathbf{I} = \mathbf{L}$ , then:

$$[S] = \langle [s] \rangle \quad \text{and} \quad \{H\} = \langle [s] \{h\} \rangle. \quad (36)$$

Applying a mean field assumption as described above is the standard procedure for linking models that span length scales. Some mean field assumptions lead to volumetric averages that constitute bounds on the computed behaviors. For the example of identical velocity gradients, it is well known that the computed properties constitute an upper bound on the stiffness (see Taylor (1938), for example). Thus, for the same change in shape for equivalent micro and macro domains, the macro stress will change by a larger amount. Similarly, one could assume that the stress is identical at both the macroscopic and microscopic scales, leading to a lower bound on the stiffness (see Asaro and Needleman (1985); Marin and Dawson (1998a,b)).

From this point the crystal scale and macroscopic scale formulations are the quite similar. The trial functions are

introduced for the velocity, leading to a matrix equations for the nodal point velocities at the end of a time step. This is a nonlinear system, involving the elastic strain at the end of the time step as well as the velocity, that is solved iteratively. The lattice orientations and slip system strengths are updated over the time step by integrating Equations 15 and 13 numerically. The numerical solution gives the nodal velocities as a function of time, together with the history of the elastic strain, lattice orientations and slip system strengths. For the macroscopic formulation, however, there is an aggregate of crystals at each point where properties are evaluated with an associated distribution of lattice orientations and slip system strengths.

### 4.3 Multiscale methodology

Bounds are often useful and may be adequate for many purposes. However, in linking scales in a multiscale simulation using averaging assumptions that bound the properties from above or below can lead to unrealistic results. Assuming that the velocity gradient at the microscopic level is identical to the macroscopic velocity gradient depletes the microscopic medium of many of its kinematic degrees of freedom. All of the crystals in a polycrystalline aggregate do not deform identically in a mode that matches the macroscopic average, but making this assumption forces that behavior on the system. In general, once this assumption is made, the stresses must be allowed to take on the values that are consistent through the constitutive model. These values need not be the same in all crystals, and generally will not be if the crystal responses are anisotropic. Thus, the stress cannot be continuous across grain boundaries for arbitrary spatial arrangements of the crystals. This may lead to difficulties when attempting to reconcile observations made on a single experiment on both the macro and micro scales.

Instead, one could choose to force the macroscopic discretization to exhibit the same apparent stiffness as the microscopic ensemble by modifying the properties. For the elastic response this would constitute reducing the moduli for the macroscopic model to compensate for the loss of kinematic degrees of freedom. We will utilize this approach in the example presented later by requiring that the change in macro stress under a prescribed deformation be the same as the micro stress for the same overall deformation and computed using the surface-traction definition of stress.

The finite elements in the macroscopic formulation provide a very natural way to convey information from the macroscopic scale to the crystal scale. Elements whose position and size correspond to crystal scale volumes (polycrystals) are chosen. The histories of the coordinates of their nodal points are extracted from the overall records. An equivalent volume of material is filled with crystal scale finite elements in which each element represents a distinct crystal. The lattice orientations of the crystals are initialized by sampling the experimentally measured distribution functions. The positions of the surfaces of the volume are then driven to move in a manner defined by the movement of the nodal coordinates over the duration of the experiment. In this way, the external shape change of the crystal scale volume, as computed from the macroscopic level, is imposed on an aggregate of grains that fills that volume. Within the volume, the deformation may be very heterogeneous from crystal to crystal.

In general, information must also be passed from the crystal scale to the continuum scale for a fully coupled formulation. Ideally, properties could be computed at finer scales and passed up to the coarser scales. However, as introduced earlier in the context of averaging, a property does not have precisely the same meaning as one crosses length scales because it does not relate precisely the same quantities. For example, the elastic modulus that relates stress to elastic strain at the crystal level is not the same quantity that relates the stress to elastic strain at the macroscopic scale, so it need not have the same value. One can compute the relation between the values of the property at the coarser scale knowing the property at the finer scale and making appropriate use of the definitions of the stress and strain measures involved, provided the conditions of smoothness discussed before are met. If the smoothness is not guaranteed, then modeling assumptions are invoked that must be assessed by comparison to experiments. In this regard, experiments that provide data at both scales are vital. Diffraction experiments with *in situ* loading provide these data.

## 5 Available Data from *In Situ* Diffraction Experiments

Diffraction measurements provide data that are crucial for understanding material behavior at the crystal scale, including the quantification of the microstructural state and the response to loading. Books are available that

collectively cover both basic and advanced topics of the subject, so we refer the reader to references by Warren (1990), Krawitz (2001) and Snyder, Fiala, and Bunge (1999) for background regarding diffraction methods and their application to polycrystalline materials.

### 5.1 Material characterization

The material used in this investigation is a super-austenitic stainless steel (AL6XN), which has a nominal composition consisting of 49 Wt% Fe, 20 Wt% Cr, 24 Wt% Ni, 6 Wt% Mo, and < 1 Wt% each of N, Mn, Si, and Cu (as per fact sheet by Allegheny Ludlum Corporation (no date)). The micrograph given in Figure 1 was obtained from a specimen etched to highlight the grain boundaries. The material is essentially single-phase (FCC) with a relatively equi-axed grain structure. The average grain size is on the order of 50  $\mu\text{m}$ . There is evidence of mechanical twins and second phase particles (referred to as the sigma phase) that are much smaller than a typical grain of the primary phase. The crystal-

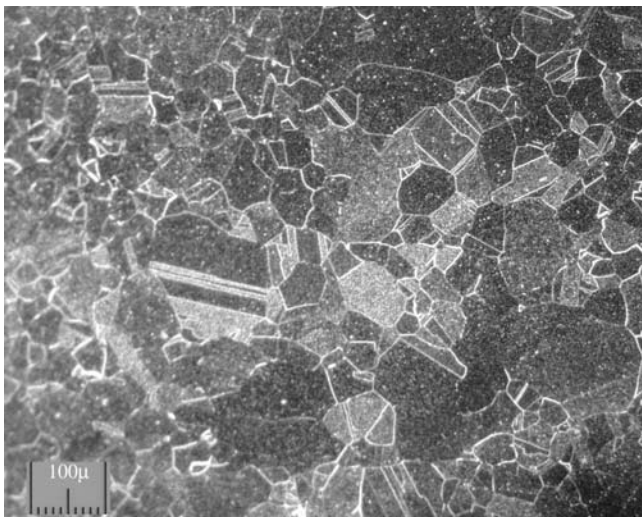


**Figure 1** : Optical micrograph of AL6XN microstructure.

lographic texture was determined by measuring several pole distributions by neutron diffraction (Figures 2) and from those constructing the ODF, shown in Figure 3 over the Rodrigues cubic fundamental region. The texture is characteristic of a mild rolling texture. The mechanical behavior under tensile loading is shown in Figure 4. The material exhibits a nearly constant strain hardening rate to large strain. There is little initial yield asymmetry, but

after loading reversals after 3% or 5% strain show a pronounced offset that persists well after the reversal.

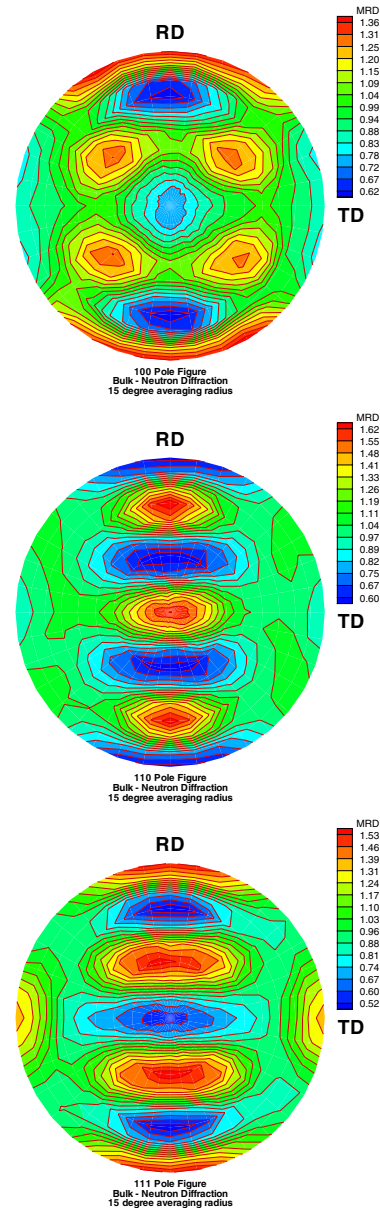


**Figure 2** : Pole figures for AL6XN obtained by neutron diffraction. (Scale is in multiples of a uniform distribution.)

### 5.2 Diffraction Measurements with In Situ Loading

It is possible to measure the macro and micro responses simultaneously using a diffractometer while loading a specimen *in situ*. Macroscopically, the load can be monitored and the strain measured over some gage section.

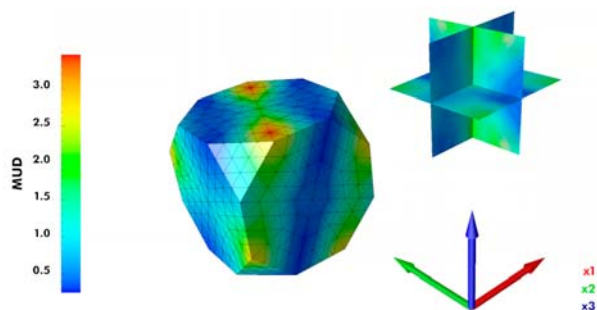


**Figure 3** : Orientation distribution function (ODF) for AL6XN determined from inversion of the measured pole distributions shown in Figure 2. (Scale is in multiples of a uniform distribution.)

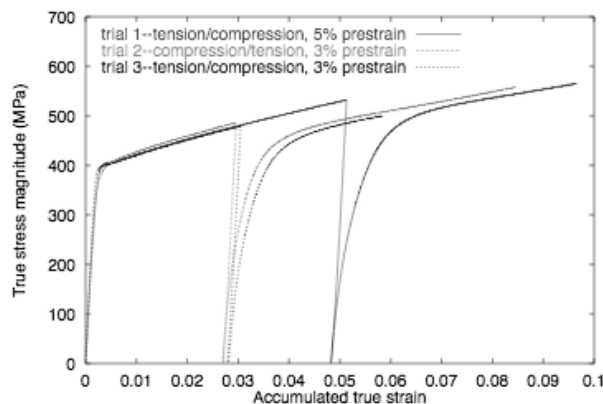


**Figure 4** : Tensile stress-strain response for AL6XN with load reversals. Quasi-static strain rate of  $\approx 10^{-3} \text{s}^{-1}$

Microscopically, diffraction peaks can be monitored for selected combinations of scattering vectors and crystallographic planes. The peaks provide extensive data regarding the microstructural state of those crystals that are within the diffraction volume and that contribute to one of the peaks by satisfying Bragg's Law.

Those attributes of the peak profiles that are particularly useful for the issues considered in this paper are the changes in peak position and peak width with changes in load. Changes in the peak intensity reflect changes in the crystallographic texture, but we'll not focus on those here. Detailed aspects of the peak profile (skewness, for example) provide opportunities to study issues like the form of the hardening equations, but again, we'll not utilize those now. Changes in the peak position are proportional to the average change in lattice spacing normal to

the associated  $hkl$ . This gives an average value of one component of the elastic strain tensor for those crystals whose crystallographic orientation lies close to the fiber parallel to the scattering vector. The changes to the peak width, for fixed experimental parameters and diffraction volume, are associated with variations in the lattice plane spacing that are due to inhomogeneities of the strain over scales associated with the grains and with the dislocations. For loading histories that involve intermittent unloading episodes during an overall large deformation the changes to the peaks provide evidence of how the macroscopic deformation is accommodated at the microscopic scale. We will employ these to assess the performance of the multiscale model.

The set-up of the diffraction instrument includes specifying slit dimensions for the incident and diffracted neutron beams. These dimensions were chosen to maximize the number of grains for meaningful polycrystalline averaging, but to avoid instrumental aberrations. For the combinations of specimens and slit dimension used here, the instrumental gauge volumes contained on the order of  $10^5$  to  $10^6$  grains. A multiwire detector was used to collect the count distribution and a Gaussian function with constant background was fitted to the measured distribution, as discussed by MacEwen, Jr., and Turner (1983) and Holden, Clarke, and Holt (1997). Gaussian functions provided good approximations to all data presented here. Neutron counting intervals were sufficiently long to provide desired level of uncertainty in the Gaussian parameters. The typical uncertainties in lattice strain was  $\pm 0.0001$ , which can be traced to the statistical quality of the fit to the neutron data. All of the *in situ* loading tests were performed on the L3 diffractometer located at the NRU research reactor, Chalk River Laboratories<sup>4</sup>, Ontario, Canada.

### 5.3 Tension and Bending Experiments

Tests were performed on two types of specimens: straight bars and curved beams. The straight bars had rectangular cross-section and were loaded in tension (Figure 5.) Specimen length was chosen to eliminate end effects within the instrumental gauge volume and to avoid interference of the neutron beam with the loading appara-

<sup>4</sup> The Chalk River Laboratories and NRU are owned and operated by Atomic Energy of Canada, Ltd. The neutron scattering facilities are owned and operated by the National Research Council, Canada (see <http://neutron.nrc.ca>)

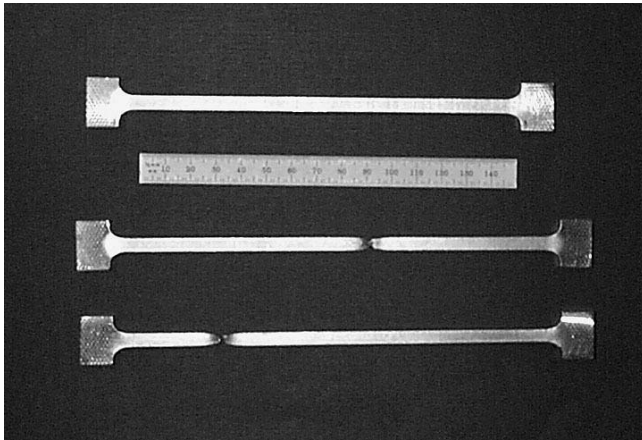


**Figure 5** : Straight bar specimen geometry. Upper bar is undeformed; lower bars are deformed.

tus. The loading programme consisted of extending the specimen under displacement control at room temperature and a nominal strain rate of  $10^{-4}\text{s}^{-1}$  to a load level close to that needed to cause the specimen to neck and fail ( $\approx 25\%$  for the stainless steel alloy studied here). At several intermediate load levels the specimens were unloaded to nearly zero load and then reloaded to continue the loading programme. During an unloading episode, the specimen was first unloaded to 95% of the target load and diffraction data were obtained. The 95% load level was chosen so as to mitigate stress relaxation from plastic deformation during the measurement process. Diffraction measurements were repeated at a near zero load level<sup>5</sup> and at the 95% reloaded level. Several peaks also were measured during the initial loading, including ones at very light load. These latter peaks served as reference values from which the initial lattice spacing parameter was established for later use in determining lattice strains from peak shifts. Peaks were measured for several combinations of scattering vector<sup>6</sup> and  $(hkl)$ :  $\{200\}$ ,  $\{220\}$ ,  $\{222\}$ , and  $\{311\}$  reflections for the axial and two transverse scattering vectors. The results for the two transverse scattering vectors are quite similar, so results are shown only for one.

The second type of specimen, a curved beam, was chosen to develop a spatially-varying stress distribution over

a length scale much larger than an individual grain (Figure 6.) By pulling the ends of the specimen apart, a state

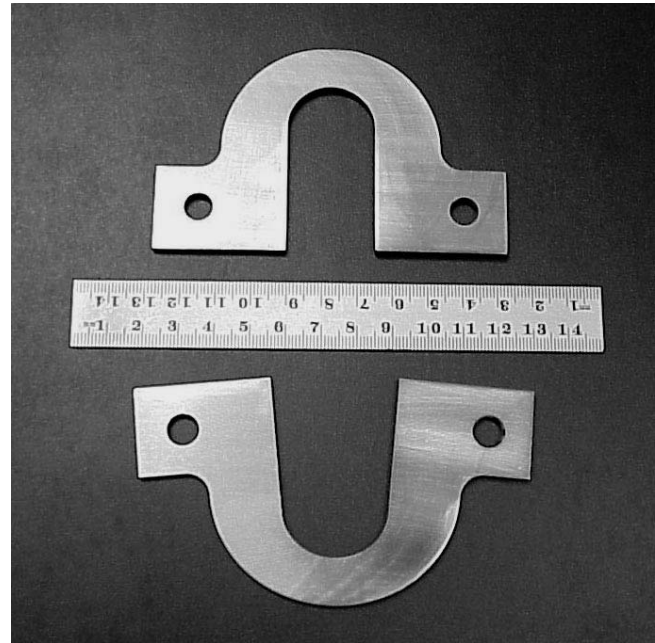


**Figure 6** : Bending specimen geometry. Upper specimen is undeformed; lower specimen is deformed.

of bending is induced in the curved section. The moment is largest at the centerplane, and consequently so is the stress. The lattice strains were measured at a number of locations along this surface, showing a distribution typical of bending. These measurements necessitated repositioning of the load frame with relation to the beam both to examine different diffraction volumes and to accommodate the relative movement of the individual diffraction volumes with respect to reference positions on the load frame as the specimen deformed. A loading programme similar to the tension tests was selected that also employs a number of loading and unloading episodes. During the unloading episodes diffraction measurements were made, but only for a more limited set of peaks. A full test, involving several unloading episodes, several diffraction volumes, and multiple crystallographic reflections, required nearly a week of beam (diffractometer) time.

## 6 Modeling the *In situ* Experiments

The simulations were performed using the finite element formulation described in previous sections and the procedures given in Dawson, Boyce, MacEwen, and Rogge

<sup>5</sup> A small tensile load was retained (50 N or  $\sim 2\text{MPa}$ ) to avoid introducing any slack in the load train.

<sup>6</sup> The scattering vector bisects the source and diffraction directions and defines the orientation of the planes for which lattice spacing data are obtained.

(2001) for simulating it in situ tests. The single crystal parameters given in Table 1. For the straight bar under axial loading, a portion of the gage section was modeled; the specimen ends were enlarged in comparison to the gage section to permit gripping, but these features were not represented. For the curved beam, the entire specimen was modeled at the macroscopic scale; polycrystal volumes at the crystal scale were defined at locations corresponding to the diffraction volumes. Details are given in the following subsections. The loading programmes measured in the experiments were applied to the specimens. In each case, the specimen was extended at constant rate until a target load was reached. At the target load, an unloading/reloading episode occurred. The procedure was continued until the full loading programme was replicated. The results at numerous points along the loading programme were saved for later post-processing to extract data comparable to that obtained from the measured diffraction peaks.

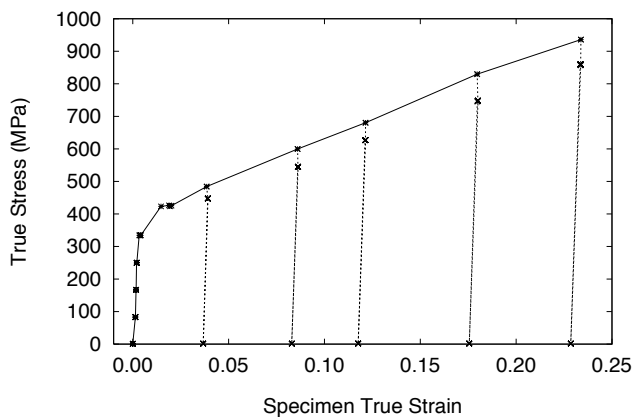


**Figure 7** : Stress-strain curve under *in situ* loading showing unloading episodes. The 'x' symbols indicate points in the loading programme at which diffraction measurements were made.

The first step in the post-processing operation is to determine which subset of the orientations should be considered active when simulating a particular diffraction peak. Any element whose orientation (accounting for crystal symmetries) is such that the designated crystal plane normal lies within a solid angle  $\Omega$  of the scattering vector is considered to be active in contributing to the simulated diffraction peak. Experimentally, only those crystals that align with the scattering vector to a high degree of res-

olution will contribute to the peak. Even with tens of thousands of elements, the simulations cannot produce the degree of resolution comparable to the experiment, so typically we must specify a larger resolution angle,  $\Omega$ , in the simulations than is set by the slit dimensions of the diffractometer. The resolution angle should be as small as possible to maximize the fidelity to the experiment, but at the same time large enough to provide meaningful statistics. The lattice strains, given by the elastic strain tensor, are averaged over that set of crystals. The component of the average strain tensor in the direction of the specified plane normal (scattering vector) is then obtained for each element. Finally, the slip system strength is averaged over the set of crystals that contribute to the peak.

### 6.1 Tension Experiments

The straight bar under axial loading produces a uniform macroscopic state of stress and strain over the central section of the gage length. Spatial variations in the stress and strain occur at the crystal scale due to the single crystal anisotropy and can be examined in the absence of the macroscopic variations with this arrangement (straight bar under axial loading). The polycrystal being modeled can be thought of as coming from any portion of the gage volume that is not affected by the end constraints. It needs only to have sufficient number of grains to be statistically significant.

A portion of the gauge section of the specimen was discretized with approximately 56,000 elements. In all of the simulations, each finite element of the mesh is an 8-noded brick and is treated as an individual crystal, and so is assigned initial values for its own orientation, slip system strength, and elastic strain tensor. All of these state descriptors are free to evolve during the course of the simulation. The crystal lattice orientations were initialized by sampling the orientation distribution function (ODF) for the specimen material. The initial value of slip system strength was taken to be constant across all elements, and the initial value of the elastic stretch tensor was taken as the identity (corresponding to zero initial lattice strain). With this level of resolution, the simulations capture stress variations between crystals. However, since the order of the elemental interpolation is low (tri-linear velocity field within crystals), stress fluctuations around dislocations are not modeled explicitly.

Boundary conditions were chosen to replicate the loading

**Table 1** : Single crystal parameters for AL6XN. ( $c_{44}$  relates the shear stress to shear strain using the mechanics convention for shear strain,  $\epsilon_{ij} = (u_{i,j} + u_{j,i})/2$ .)

	$c_{11}$	$c_{12}$	$c_{44}$	
	(GPa)	(GPa)	(GPa)	
	190.9	125.5	230.3	
$\dot{\gamma}_0$	$m$	$h_0$	$g_0$	$g_s$
( $\frac{1}{s}$ )	(-)	(MPa)	(MPa)	(MPa)
1.0	0.02	300	160	2000

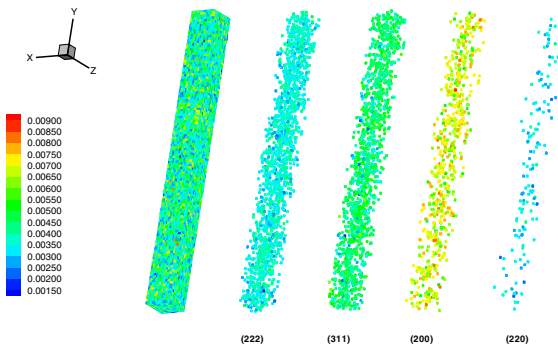


**Figure 8** : Axial lattice strains at beginning of the last unloading episode. The crystals contributing to each measured reflection are plotted separately. Differences in the numbers of crystals are due to a combination of the different multiplicity of the various crystal planes and the crystallographic texture.

of crystals within the gauge section of the tensile specimen. One end of the mesh was constrained in the axial direction while a specified axial velocity was imposed on the other end; zero shear tractions were imposed on both ends. Two adjacent lateral sides were traction free, while on the other two a symmetry condition was imposed. The velocity on the end was prescribed to follow the loading programme of the experiment. At each point at which neutron diffraction measurements were made, the current orientation, slip system strength and elastic strain information for each element was written to a file. These raw simulation results were subsequently post-processed to obtain quantities analogous to those obtained experimentally. The stress strain curve is shown in Figure 7. Finite element meshes showing lattice strains on crystals of several sets are shown in Figures 8 and 9.

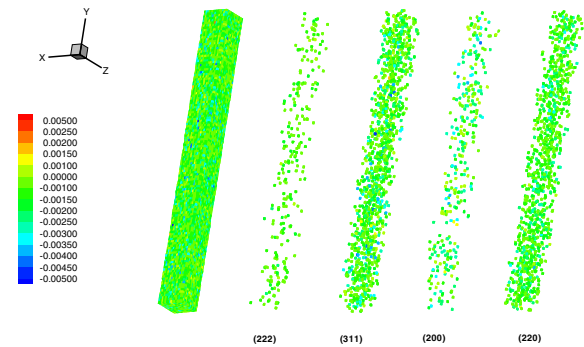


**Figure 9** : Transverse lattice strains at beginning of the last unloading episode. The crystals contributing to each measured reflection are plotted separately. Differences in the numbers of crystals are due to a combination of the different multiplicity of the various crystal planes and the crystallographic texture.

The computed lattice strains for the axial and one transverse scattering vector are shown in Figure 10 and 11, for several crystallographic planes. In the axial direction, lattice strains reach values between 0.3% and 0.8%. The transverse strains are smaller and opposite in sign, and are consistent with an average Poisson's ratio of  $\approx 0.25$ . Also shown in the figures are the lattice strains taken from experiments. In general, the comparisons are very good, especially when comparing across the various  $hkl$ 's. The strains of the 400 crystals are about twice those of the 222 crystals, which is captured well by the simulations. The main deficiency of the simulations is the underprediction of the effect of the elastic anisotropy. The strain on unloading is depends less on  $hkl$  in the simulation than was observed in the experiments.

The standard deviations of the computed lattice strain distributions are presented in Figure 12 for the axial and a transverse direction. In the axial direction, the standard deviations are about 10% of the average values and the lattice strain in the transverse direction show larger computed variations.

## 6.2 Bending Experiments

The curved beam develops macroscopic gradients in the stress and strain distributions when its ends are pulled in opposite directions. The state of loading resembles that of pure bending, but is not exactly that condition owing to axial component that arises from the method of loading

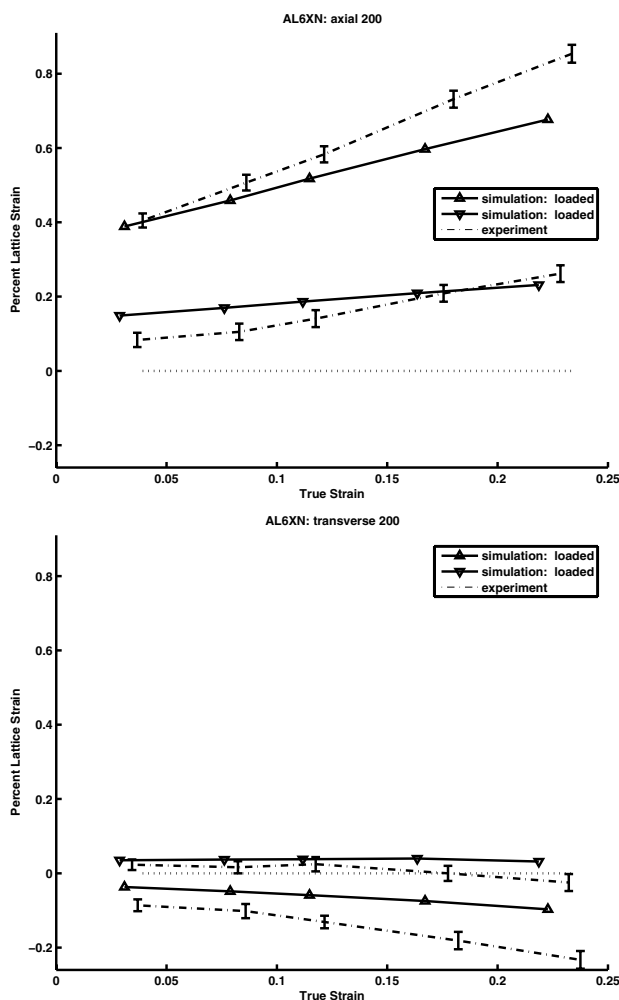


**Figure 10** : Comparison of the computed and measured lattice strains for 200 crystals. Upper: axial strains; lower: transverse strains. Experimental points are shown with estimated error bars.

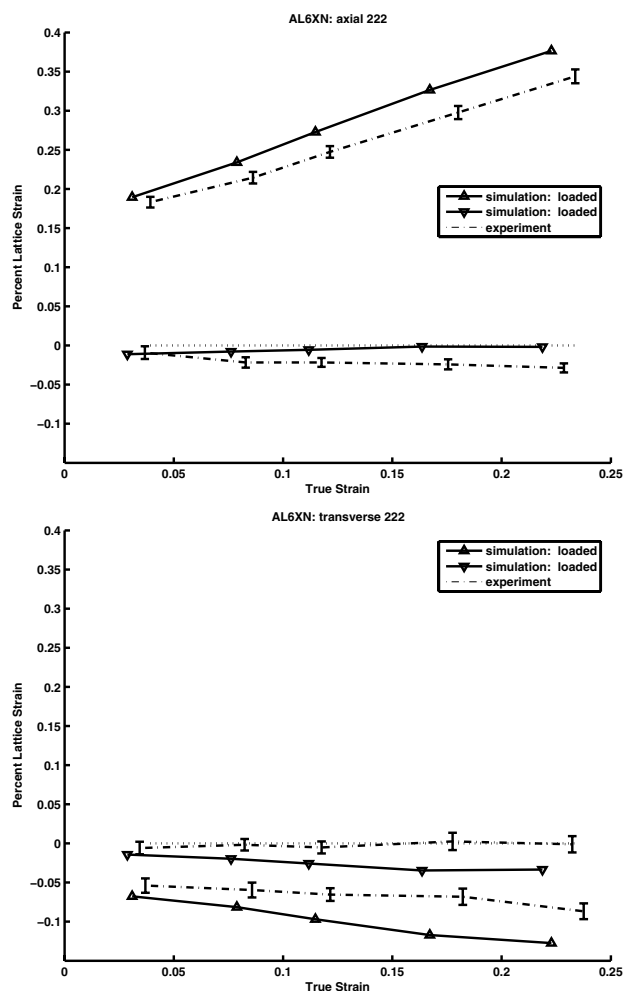


**Figure 11** : Comparison of the computed and measured lattice strains for 222 crystals. Upper: axial strains; lower: transverse strains. Experimental points are shown with estimated error bars.

the specimen. The finite element mesh for a symmetric half of the specimen at the macroscopic scale is shown in Figure 13. This mesh contains a total of 1548 elements, with each element having assigned a total of 128 crystal orientations to define the texture within it. The initial values for the orientations were defined from a random sampling of the orientation distribution function.

The measured loading programme, shown in Figure 14, was applied to the curved beam (macroscopic) mesh. This programme includes a total of 7 unloading/reloading episodes, as well as the final unloading sequence. This history was sufficient to produce plastic deformations along the centerplane where the moment is highest, imparting a permanent shape change to the

specimen, as shown in Figure 13. All of the latter unloading episodes involved unloading from an elastoplastic condition existing when a target load was reached. The macroscopic stress distributions in the loaded and unloaded conditions of the final unloading episode are shown in Figure 15.

Elements in the macroscale mesh are comparable to, but somewhat smaller than, the experimental diffraction volumes. From the macroscopic scale results, loading histories for elements along the centerplane were extracted, as shown in Figure 17. Specifically, the velocity history of surface of a macroscopic element was imposed on the corresponding surface of the crystal scale mesh, thereby forcing the boundary of the polycrystal to move in the

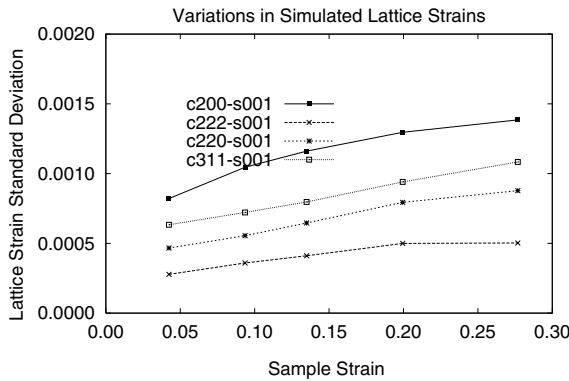


**Figure 12 :** Standard deviations of the computed transverse lattice strains for the various measured crystal reflections. Designation code of curves given in the key refer to the crystallographic plane and sample direction, respectively.

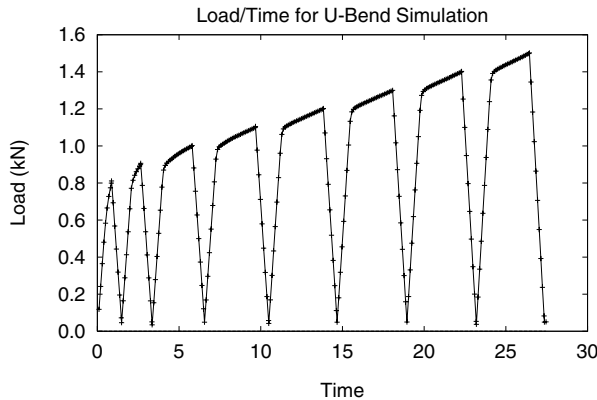
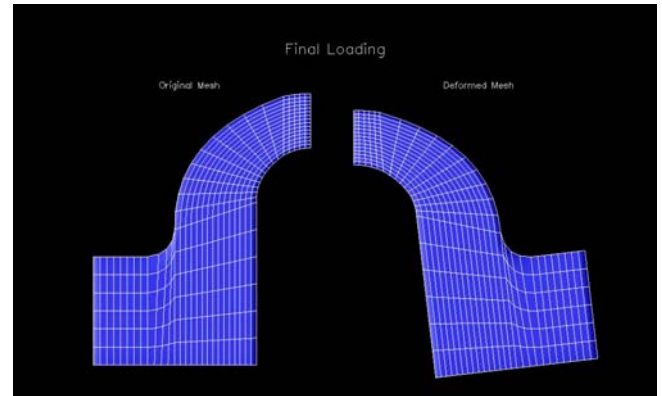


**Figure 14 :** Load history on bending specimen. Scale is in seconds; hold times for diffraction measurements have been omitted.

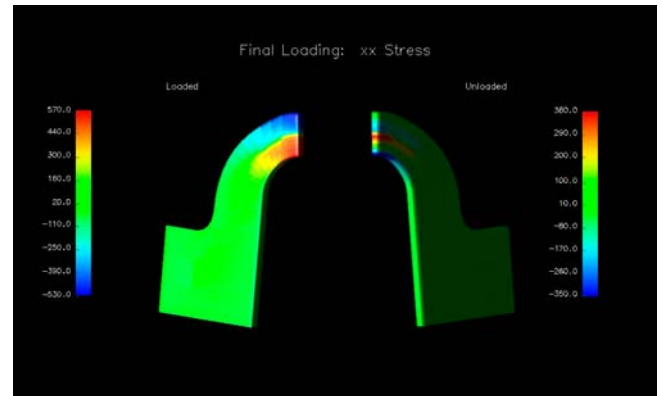
same way as the boundary of the macroscopic element. Figure 16 shows one of the crystal scale meshes. It contains 1000 elements with each element corresponding to an individual crystal; the complete mesh, or polycrystal, coincides with one of the elements along the centerplane of the macroscopic mesh.

Figure 17 shows the history of 15 elements adjacent to the centerplane. These span the same cross section as examined experimentally, although the centroids of the simulation and experimental diffraction volumes do not exactly coincide.

Comparisons between measured and computed lattice strains are shown for the final complete unloading episode. For both the loaded and unloaded states, lattice strains for 004 crystals are shown in Figure 18 and strains



**Figure 13 :** Undeformed and deformed meshes for the bending application.



**Figure 15 :** Normal stress components at the initiation (left) and conclusion (right) of the final unloading episode.

for 222 crystals are shown in Figure 19. One can readily see the bending profile expected for a plastic hinge of a strain hardening material in the loaded state and the subsequent residual profile for the unloaded state. The computed strains are somewhat higher, but the difference between the loaded and unloaded states are compare well between experiment and simulation. The 004 strains are considerable larger (factor of two) than the 222 strains, a trend which is captured by the simulation. Probably the most notable difference between simulation and experiment is the sharpness of the computed profile near the neutral axis in the unloaded state. This trend is much more muted in the experiment. The size of the diffraction volume may influence this difference. By averaging lattice strains in adjacent elements, we also show the result

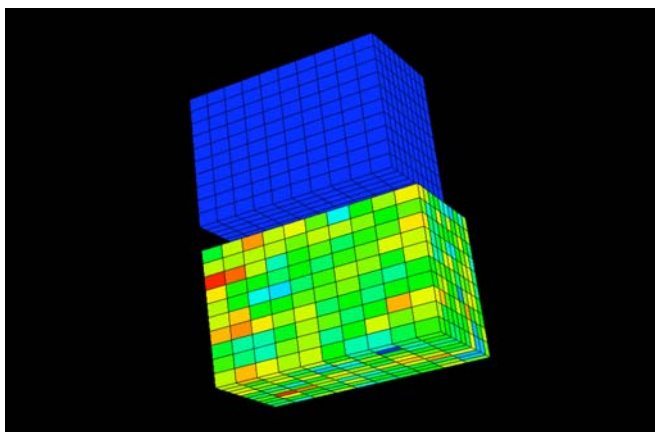


**Figure 16** : Diffraction volume (microscopic) finite element mesh for the bending specimen simulations. Upper figure shows the undeformed mesh; the lower figure shows the final mesh where color indicates relative magnitude of the  $xx$  component of stress.

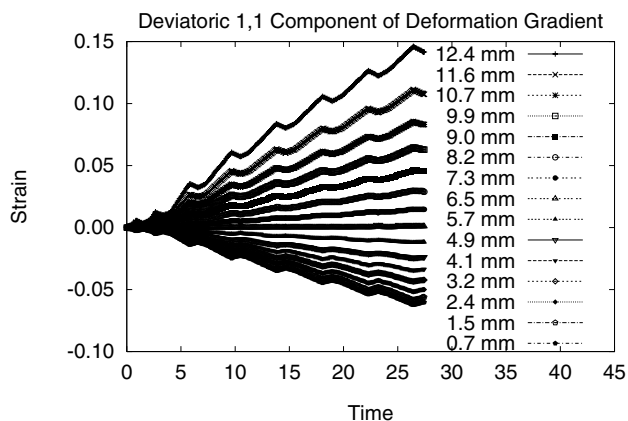


**Figure 17** : Deformation gradient histories extracted from the continuum scale simulation and applied to the crystal scale meshes corresponding to diffraction volumes along the specimen centerplane. Scale is in seconds; hold times for diffraction measurements have been omitted.

corresponding to enlarged diffraction in the simulations. As expected, these compare more closely to experiments.

The macroscopic scale simulation imposed the measured displacement history to the specimen at the points where it is held by the load-frame fixtures. Each unloading episode is triggered by reaching a target load used in the experiment. During the unloading episode itself, the direction of the displacement is reversed until the load is close to zero, just as in the experiment. Thus, at the

macroscopic scale, reaching an unloaded configuration occurs by control of the boundary conditions. The precise amount of displacement needed to accomplish the unloading depends on details of the macroscopic model, including the mesh resolution, the representation of the texture within each element, and the elastic moduli. The motion of an element that is assumed to represent a diffraction volume is consistent with the macroscopic motion that unloads the specimen. This motion is imposed on the crystal scale aggregate. Because the material within the volume is represented differently, that same motion may not produce the same stress history. This will depend on how effectively the averaging procedure that serves as the basis for computing properties at the macroscopic scale captures the response of the polycrystal. Because the macroscopic motion is not homogeneous, the stresses in the macroscopic elements will not individually drop to zero on unloading of the specimen. Thus a test of how closely the two scales coincide in the aggregate behaviors can be based on whether or not the distribution of crystal scale stresses are self-equilibrating and leave the specimen in equilibrium after the loads have been removed according to the macroscopic scale. This cannot be determined from Figures 18 and 19 as each give only a subset of all of the crystals. However, the stress distribution based on stresses for the entire polycrystal (Figure 20) at each station does indicate that the continuum and crystal scale stress distributions before and after unloading compare closely. Note, however, that the macroscopic stress change is consistently larger than the microscopic change. This illustrates that the effect of not satisfying the continuity requirement at the crystal scale that is imperative to have an exactly equivalent stress across the scales. The net effect is that the stiffnesses are not identical, with the crystal scale response being more compliant. However, the differences are relatively small in this case so that the distributions compare well.

## 7 Peak Width Correlations

The influence of the polycrystalline microstructure on peak width has been investigated from a number of perspectives. It is widely recognized that the finite size of diffraction domains and irregularities in the spacing of atoms within domains contribute to peak width. These often are referred to as size broadening and strain broadening, respectively. Warren and Averbach (1950) de-

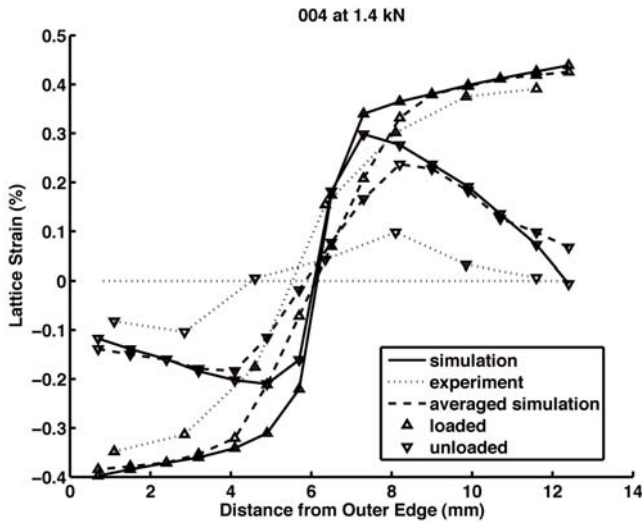


**Figure 18 :** Comparisons of measured and computed lattice strains for crystals having a 004 direction aligned with the specimen  $x$ -direction. Loaded and unloaded states are shown.

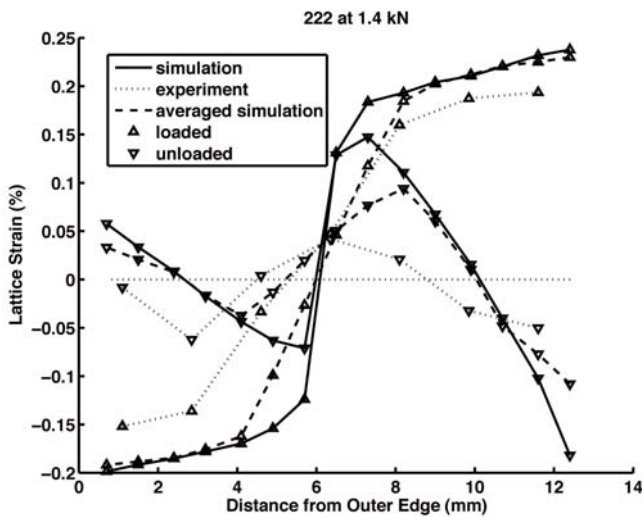


**Figure 19 :** Comparisons of measured and computed lattice strains for crystals having a 222 direction aligned with the specimen  $x$ -direction. Loaded and unloaded states are shown.

veloped a procedure based on Fourier analyses of the peak distributions for separating the influences of size and strain on width based on each one's dependence on Bragg angle. Construction of a Williamson-Hall plot, see Williamson and Hall (1953), provides another approach for estimation of the size and strain contributions to the peak profiles. The accuracy of these methods is limited

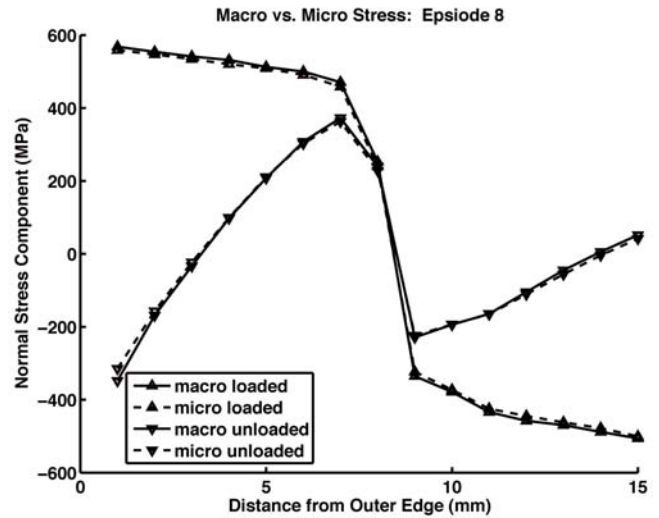


**Figure 20 :** Normal stress component ( $\sigma_{xx}$ ) distributions across the centerplane before and after unloading for the continuum and crystal scales.

by the influence of strain anisotropy (Ungar, 2001). Investigations that focus particularly on the evolution of width with plastic straining are limited, however. Smith and Webster (1997) correlated peak width with plastic strain for aluminum and steel alloys. Mohamed, Bacroix, Ungar, Raphanel, and Chauveau (1997) measured broadening of six crystals within a rolled copper multicrystal by X-ray diffraction. Baczmanski and coworkers (Baczmanski, Braham, Lodini, and Wierzbanski, 2000) compared measured changes in peak width to ones inferred from model computations, noting the correlation between peak width and dislocation density. Weisbrook, Gopalaratnam, and Krawitz (1995) compared trends computed using finite element analyses to ones observed from neutron diffraction experiments for thermal loading of tungsten-nickel composite materials.

A correlation between the experimental peak width and the simulated strain hardening has been drawn from the tension test results presented earlier. A connection between the broadening of the Bragg peaks and the evolution of the slip system strength is anticipated because both the peak width and the strength can be related to the dislocation density. Because both are proportional to the square root of the dislocation density, we expect to observe a direct dependence between increases in the peak width and elevation of the slip system strength. (Peak width also is influenced by the instrument. As the instrumental settings are the same for each test, contributions

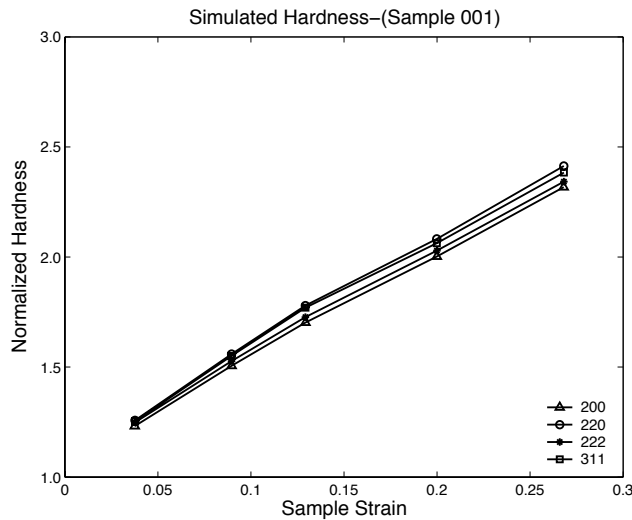


**Figure 21** : Evolution of slip system hardness for crystals having various directions aligned with the specimen transverse direction.

to the width from instrumental sources are assumed to be unchanging over the course of a test.) The average slip system strengths exhibit similar trends for all the scattering directions, with one transverse direction shown in Figure 21. For the correlation between measured broadening and computed strengthening, the contributions to peak broadening from variations in crystal lattice strain is subtracted from the total increase in peak width. The difference is attributed to the dislocation density increase and correlated with it using:

$$f(\theta)\beta_d = b_1 + b_2g^* \tag{37}$$

where  $\beta_d$  is the dislocation-based increase in the peak width and  $g^*$  is the normalized slip system strength (computed as the ratio of the average slip system strength in the diffracting crystals to the initial slip system strength). Results of the regression are reported in Table 2. A fairly consistent value of about 0.0032 is determined for all three scattering directions. The plot of the dislocation-based broadening,  $\beta_d$ , after scaling by the cosine of the Bragg angle, versus the normalized slip system strength is shown in Figure 22. The correlation was not constrained to force the condition that the excess peak width is zero where the normalized hardness is unity, so it is inaccurate in regions of very little plastic straining.

We employ this correlation to better understand the quality of the comparisons made between the bending experiment and corresponding simulations. The computed

**Table 2** : AL6XN Correlation Coefficients

sample	$c_1$	$c_2$	Correlation
100	1.42e-5	-7.9e-6	0.7642
010	4.43e-6	7.5e-6	0.9104
001	7.75e-6	-4.3e-7	0.9379
sample	$b_1$	$b_2$	Correlation
100	-1.6e-6	0.0032	0.7797
010	-0.0014	0.0034	0.8960
001	-0.00087	0.0032	0.9430

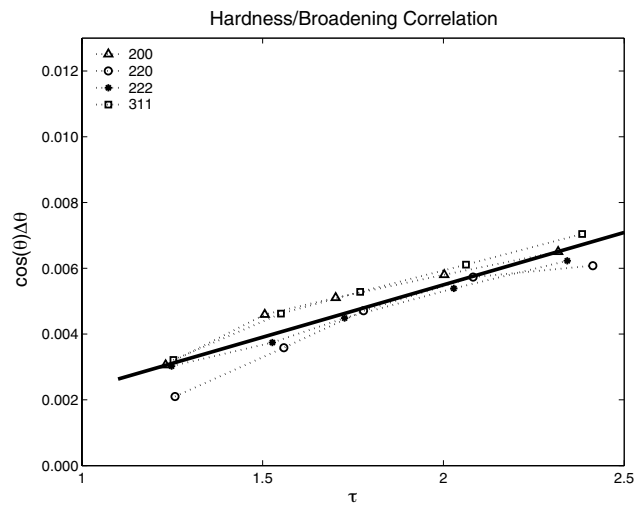


**Figure 22** : Correlation of the normalized slip system strength with evolution of peak width for crystals having various crystallographic directions aligned with the specimen transverse direction.

strain hardening across the centerplane is greatest at the inner and outer radii. Around the neutral axis, there is little or no plastic deformation and consequently no hardening. Using the correlation given by Equation 37 and the computed changes in strength, we compute the anticipated distribution of excess peak width and compare to the distribution measured from experiment. The comparison is quite close, as shown in Figure 23. Recall, however, that the principal difference between the lattice strain profiles was near the neutral axis where the simulations give a sharp profile, but the experimental profiles are muted. We also show in Figure 23 the change in peak width upon unloading as measured in the experiment. The changes on unloading are greatest near the neutral axis of bending, coinciding with the region of rapid changes in lattice strain computed in the simu-

lations. Thus while the comparisons are good over the entire section, they are only valid away from the neutral axis. At the inner and outer radii the plastic strains are sufficiently large to induce substantial change in the peak width and the correlation is reliable. In contrast, at the neutral axis the plastic strains are small and the excess peak width is over-predicted. Experimentally, the peak width is enlarged not because the dislocation density arises, but rather that the lattice strains vary from one side of the diffraction volume to the other. There is apparent agreement at the neutral axis because the computation uses the correlation where it is inaccurate and the measurement is influenced by heterogeneous elastic strains over the gage volume in the experiments. The correlation error can be rectified by imposing a constraint on the parameters in Equation 37. The experiment can be improved by decreasing the size of the diffraction volume. However, this is limited by the grain size of the material, pointing to the modeling constraint in a two-scale formulation such as that used here: one cannot employ h-type refinement to macroscopic scale that requires elements with dimensions comparable to the crystal dimension.

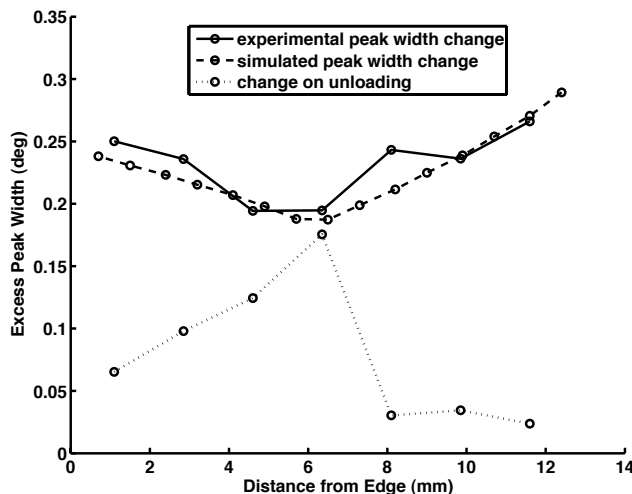


**Figure 23** : Comparison of simulated and measured peak width evolution in crystals having a 222 direction aligned with the specimen  $x$ -direction.

## 8 Discussion

We focus on two issues that arise in multi-scale formulations. One is the consistency of the stiffness of comparable volumes of material across scales. The second is

related to the limitations imposed by gradients in a field (the stress, for example) at one scale on the response at another scale. The former is important because information regarding the stress and deformation is to be passed between the models at each scale. If the motion at a point of the larger scale is imposed on a representative volume at the smaller scale then it is possible that the same change in stress will not be predicted. This occurs because the conditions needed to convert an integration over the volume to an integration over its surface are not fully met, as discussed in Section 3. In fact, the use of finite element formulations with  $C^0$  continuity for the velocity or displacement fields means that volume-averaged crystal scale stress in general cannot equate to the macrostress. Modeling approximations are made in lieu of the identity that is desired. Physical attributes of the system will dictate how elaborate the averaging methods must be for the approximation to be accurate. Nevertheless, consistency of the responses is not guaranteed *a priori* and case-by-case checks are required. In the formulation presented here, the representation of each crystal with a single brick element is relatively coarse. In this case, the crystals respond in a manner that is similar to the Taylor assumption imposed at the macroscopic level, giving reasonably comparable behavior stiffness between the two scales. However, for more highly resolved crystals, we would not expect this assumption to continue to hold necessarily.

The second issue was illustrated using the comparison of measured and computed peak broadening. The actual diffraction volume in the experiment was large enough to exhibit an influence of the stress gradient. Changes in the macroscopic load during unloading altered the peak width while the dislocation density remained essentially unchanged. This implies that the macroscopic finite elements should be smaller in size than the diffraction volume if the stress is not to vary substantially over the element. However, there are lower limits to the size of the macroscopic elements. They cannot be smaller than the volume needed to contain statistically meaningful number of grains. As with the first issue, this size is material dependent as the grain dimension can be anywhere in the range of nanometers to millimeters for many alloys. One can imagine rules-of-thumb, however, based on the ratio of grain size to feature size in the components being modeled with the macroscopic scale formulation.

## 9 Closing Remarks

Progress in simulating the deformations of polycrystalline solids has progress substantially over the past 25 years. The capabilities exist to embed detailed descriptions of the material structure explicitly in the mechanics formulations and to base the mechanical properties in part of those descriptions. The material structure can evolve with the continuing deformation and thus dynamically influence how a process will progress. The material description may include features of the structure that are readily observed by experiment, thus providing the opportunity to more rigorously validate models and to diagnose points of discrepancy between predicted and observed responses. This represents a significant advance over the capabilities first proposed and tested more than two decades ago. This progress, including the example of it presented in this paper, is indicative of positive influence that Dr. Astill had in the formative years of the discipline. A more impressive indicator, we believe, is that the expectations for the area are higher now than they were twenty years ago. We expect that computational mechanics will play a major role in improving engineering alloys, in understanding biomaterials, and in interpreting geological records. We add our appreciation to that of many others for the thoughtful efforts of Dr. Astill for cultivating such a rich and stimulating discipline.

**Acknowledgement:** Support for this work has been provided by the Office of Naval Research under contract N00014-03-1-0250. Neutron diffraction experiments were performed on a National Research Council (Canada) neutron diffractometer located at the NRU Reactor of AECL (Atomic Energy of Canada Limited). Computing resources were provided by the Cornell Theory Center. The authors thank members of the Deformation Processes Laboratory at Cornell University for their helpful suggestions and comments. Reverse yield experiments were performed by Joel Bernier; micrographs were prepared by Brian Sidle.

## References

**Allegheny Ludlum Corporation** (no date): Stainless steel al-6xn alloy. Technical Data Blue Sheet, no date.

**Asaro, R.; Needleman, A.** (1985): Texture development and strain hardening in rate dependent polycrystals.

*Acta metallurgica*, vol. 33, no. 6, pp. 923–953.

**Baczmanski, A.; Braham, C.; Lodini, A.; Wierzbanski, K.** (2000): Evolution of microstresses in plastically deformed duplex steels. *Materials Science Forum*, vol. 347–347, pp. 253–258.

**Beaudoin, A. J.; Dawson, P. R.; Mathur, K. K.; Kocks, U. F.; Korzekwa, D. A.** (1994): Application of polycrystal plasticity to sheet forming. *Computer Methods in Applied Mechanics and Engineering*, vol. 117, pp. 49 – 70.

**Dawson, P.; Boyce, D.; MacEwen, S.; Rogge, R.** (2001): On the influence of crystal elastic moduli on computed lattice strains in aa5182 following plastic straining. *Materials Science and Engineering A*, vol. 313, no. 1–2, pp. 123 – 144.

**Dawson, P. R.** (1984): A model for the hot or warm working of metals with special use of deformation mechanism maps. *International Journal of Mechanical Sciences*, vol. 26, no. 4, pp. 227 – 224.

**Dawson, P. R.** (1987): On modeling of mechanical property changes during flat rolling of aluminum. *International Journal of Solids and Structures*, vol. 23, no. 7, pp. 947–968.

**Eggert, G. M.; Dawson, P. R.** (1987): On the use of internal variable constitutive equations in transient forming processes. *International Journal of Mechanical Sciences*, vol. 29, no. 2, pp. 95–113.

**Hill, R.** (1979): Theoretical plasticity of textured aggregates. *Math. Proc. Camb. Soc.*, vol. 75, pp. 179–191.

**Holden, T. A.; Clarke, A. P.; Holt, R. A.** (1997): Neutron diffraction measurements of intergranular strains in monel-400. *Metallurgical and Materials Transactions A*, vol. 28A, pp. 2565 – 2575.

**Kocks, U. F.; Tome, C. N.; Wenk, H.-R.** (1998): *Texture and Anisotropy*. Cambridge University Press.

**Krawitz, A.** (2001): *Introduction to Diffraction in Materials Science and Engineering*. Wiley-Interscience.

**MacEwen, S.; Jr., J. F.; Turner, A.** (1983): The use of time-of-flight neutron diffraction to study grain interaction stresses. *Acta Metallurgica*, vol. 31, no. 5, pp. 657–676.

- Marin, E.; Dawson, P.** (1998): Elastoplastic finite element analyses of metal deformations using polycrystal constitutive models. *Computer methods in applied mechanics and engineering*, vol. 165, pp. 23–41.
- Marin, E.; Dawson, P.** (1998): On modeling the elastoviscoplastic response of metals using polycrystal plasticity. *Computer methods in applied mechanics and engineering*, vol. 165, pp. 1–21.
- Mathur, K. K.; Dawson, P. R.** (1987): On modeling damage evolution during the drawing of metals. *Mechanics of Materials*, vol. 6, pp. 179–196.
- Mathur, K. K.; Dawson, P. R.** (1989): On modeling the development of crystallographic texture in bulk forming processes. *International Journal of Plasticity*, vol. 5, pp. 67 – 94.
- Mohamed, G.; Bacroix, B.; Ungar, T.; Raphanel, J. L.; Chauveau, T.** (1997): Experimental and numerical determination of intragranular work hardening in a cold rolled multicrystal. *Materials Science and Engineering A*, vol. 234-236, pp. 940–943.
- Nemat-Nasser, R.; Hori, M.** (1999): *Micromechanics: Overall Properties of Heterogeneous Materials*. North-Holland.
- Raabe, D.; Roters, F.; Barlat, F.; Chen, L.-Q.** (2004): *Continuum Scale Simulation of Engineering Materials*. Wiley-VCH.
- Smith, D. J.; Webster, G. A.** (1997): The measurement of prior plastic deformation in metallic alloys using the neutron diffraction technique. *Journal of Strain Analysis*, vol. 32, pp. 37–46.
- Snyder, R. L.; Fiala, J.; Bunge, H. J.** (1999): *Defect and Microstructure Analysis by Diffraction*. Oxford Science Publications.
- Taylor, G.** (1938): Plastic strain in metals. *Journal of the Institute of Metals*, vol. 62, pp. 307–324.
- Ungar, T.** (2001): Dislocation densities, arrangements and character from x-ray diffraction experiments. *Materials Science and Engineering A*, vol. 309-310, pp. 14–22.
- Warren, B. E.** (1990): *X-Ray Diffraction*. Dover Publications, New York.
- Warren, B. E.; Averbach, B. L.** (1950): Missing title. *Journal Applied Physics*, vol. 21, pp. 595–xxx.
- Weisbrook, C. M.; Gopalaratnam, V. S.; Krawitz, A. D.** (1995): On the use of finite element modeling to interpret diffraction peak broadening from elastic strain distributions. *Materials Science and Engineering*, vol. A201, pp. 134–142.
- Williamson, G. K.; Hall, W. H.** (1953): Missing title. *Acta Metallurgica*, vol. 1, pp. 22–31.

